ACS NANO Caltech Library

Subscriber access provided by Caltech Library

Article

Biomolecular Ultrasound Imaging of Phagolysosomal Function

Bill Ling, Justin Lee, David Maresca, Audrey Lee-Gosselin, Dina Malounda, Margaret B. Swift, and Mikhail G. Shapiro

ACS Nano, **Just Accepted Manuscript** • DOI: 10.1021/acsnano.0c05912 • Publication Date (Web): 09 Sep 2020

Just Accepted

Biomolecular Ultrasound Imaging of Phagolysosomal Function

Authors:

Bill Ling[1], Justin Lee[2], David Maresca[1], Audrey Lee-Gosselin[1], Dina Malounda[1], Margaret B. Swift[1], Mikhail G. Shapiro[1]*

Affiliations:

1. Division of Chemistry and Chemical Engineering, California Institute of Technology, Pasadena, California, 91125, United States

2. Division of Biology and Bioengineering, California Institute of Technology, Pasadena, California, 91125, United States

*Corresponding author. Email: mikhail@caltech.edu

Abstract

Phagocytic clearance and lysosomal processing of pathogens and debris are essential functions of the innate immune system. However, the assessment of these functions *in vivo* is challenging because most nanoscale contrast agents compatible with non-invasive imaging techniques are made from non-biodegradable synthetic materials that do not undergo regular lysosomal degradation. To overcome this challenge, we describe the use of an all-protein contrast agent to directly visualize and quantify phagocytic and lysosomal activities *in vivo* by ultrasound imaging. This contrast agent is based on gas vesicles (GVs), a class of air-filled protein nanostructures naturally expressed by buoyant microbes. Using a combination of ultrasound imaging, pharmacology, immunohistology and live-cell optical microscopy, we show that after intravenous injection, GVs are cleared from circulation by liver-resident macrophages. Once internalized, the GVs undergo lysosomal degradation, resulting in the elimination of their ultrasound contrast. By non-invasively monitoring the temporal dynamics of GV-generated ultrasound signal in circulation and in the liver and fitting them with a pharmacokinetic model, we can quantify the rates of phagocytosis and lysosomal degradation in living animals. We demonstrate the utility of this method by showing how these rates are perturbed in two models of liver dysfunction: phagocyte deficiency and non-alcoholic fatty liver disease. The combination of proteolytically-degradable nanoscale contrast agents and quantitative ultrasound imaging thus enables non-invasive functional imaging of cellular degradative processes.

Keywords

ultrasound, contrast agents, phagocytosis, lysosomes, liver disease, reticuloendothelial system

The reticuloendothelial system (RES), also known as the mononuclear phagocyte system, is a network of phagocytic immune cells that is essential for organismal development and homeostasis; malfunctions in this system may lead to increased susceptibility to infections[1,2] and are associated with the pathogenesis of a variety of conditions, including neurodegeneration,[3,4] chronic liver disease[5] and many others.[6] Cells of the RES, such as monocytes, macrophages and dendritic cells, continuously sample their surroundings, mediating the recognition and clearance of abnormal and senescent cells, debris and foreign particulates.[7,8] Additionally, they interface with the adaptive immune system by presenting lysosomally-processed antigens to lymphocytes and secreting cytokines to stimulate the proper inflammatory response.[8-10] Phagocytosis and lysosomal degradation are thus vital processes of RES-mediated immunoregulation.

Non-invasive functional imaging of phagocytosis and lysosomal activities will enable early detection and monitoring of non-alcoholic fatty liver disease (NAFLD) and other conditions resulting from RES dysfunction. NAFLD currently affects over 25% of the global population and its progression is associated with chronic hepatic inflammation.[11] Due to the large patient population and broad range of outcomes which include hepatitis, cirrhosis, fibrosis and hepatocellular carcinoma, rapid and non-invasive diagnostic methods are needed to stratify patients into defined risk groups.[5,11] Ultrasound is well suited for this task due to its wide availability, portability, low operational costs and high tissue penetrance.[12] Based on *in vitro* observations that pro-inflammatory macrophages suppress phagocytosis[13] and lysosomal degradation,[14,15] one would expect livers in patients with NAFLD to exhibit reduced accumulation and extended persistence of intravenously-administered nanoscale contrast agents. Indeed, clinical studies have confirmed the former.[16,17] However, the latter cannot be evaluated with currently available technologies because agents compatible with non-invasive imaging modalities are typically made from synthetic materials which do not undergo regular lysosomal degradation.[7,8]

Here, we describe the use of an all-protein nanoscale contrast agent to visualize and quantify both phagocytic clearance and lysosomal degradation *in vivo* using ultrasound imaging.

This contrast agent is based on gas vesicles (GVs), a class of air-filled protein nanostructures natively formed inside certain photosynthetic microorganisms as a means to regulate buoyancy.[18] GVs comprise a rigid, 2 nm-thick protein shell allowing the free exchange of gas but preventing the internal condensation of liquid water, thereby forming a thermodynamically stable capsule of air with a hydrodynamic diameter of approximately 250 nm.[19] They are easily isolated from cultures of their native cyanobacterial hosts[20] and can be expressed heterologously in bacteria[21,22] and mammalian cells.[23] Because sound waves are strongly reflected by air-water interfaces, GVs have been developed as contrast agents for ultrasound imaging.[19, 24-27] Due to their innate stability, GVs are able to withstand repeated insonation without loss of contrast.[19] However, when the GV shell is compromised by mechanical or chemical disruption, the gaseous contents it encloses rapidly and irreversibly dissolve into the surrounding media, leading to the elimination of ultrasound contrast.[19,21,27]

Based on their nanoscale dimensions and all-protein composition, which distinguishes them from other classes of ultrasound contrast agents,[28-31] we hypothesized that we could use GVs as a contrast agent to non-invasively visualize the phagocytic and lysosomal functions of hepatic macrophages *in vivo*. Previous studies have shown that intravenously injected GVs are rapidly taken up by the liver.[32,33] If this uptake is mediated by macrophages and the internalized GVs undergo lysosomal proteolysis, this would manifest in the initial transfer of ultrasound contrast from the bloodstream to the liver, followed by its elimination with kinetics representative of natural RES clearance and degradation. Measurement of these processes would thus provide a quantitative picture of the complete phagocytic and lysosomal degradation pathways. This rate-based approach would improve upon previous Kupffer cell imaging techniques[16,34-36] which are limited to the assessment of phagocytosis. In this study, we test this hypothesis by visualizing the temporal dynamics of GV ultrasound contrast in the blood and liver, establishing the cellular and molecular pathways mediating GV uptake and degradation, and developing a pharmacokinetic model to parametrize RES activity from hemodynamic and liver ultrasound signals. Finally, we

demonstrate the diagnostic utility of functional imaging of macrophage phagolysosomal activity in two models of liver disease: clodronate-mediated macrophage deficiency and diet-induced NAFLD.

Results and Discussion

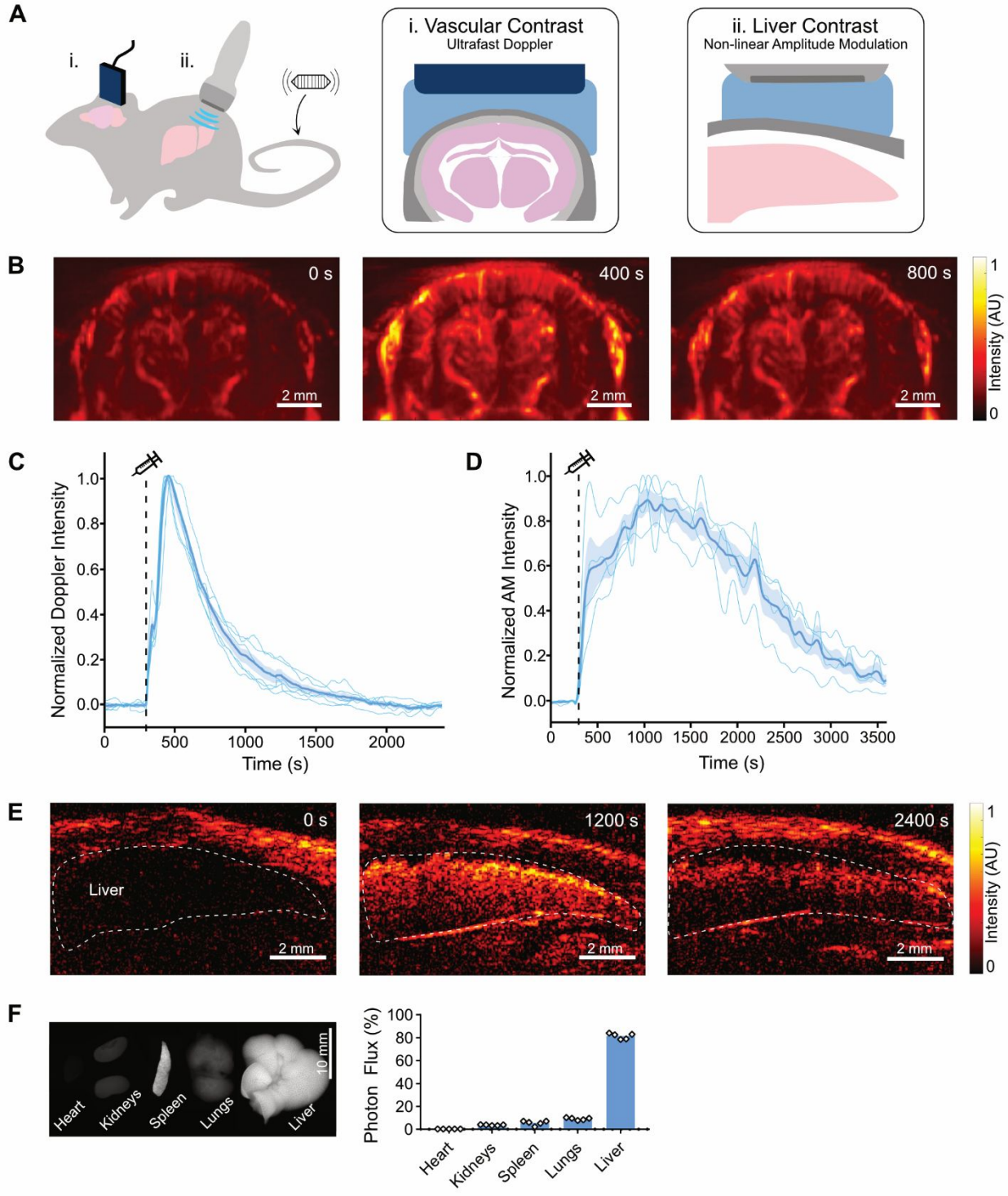

Figure 1: Non-invasive ultrasound imaging of GV clearance and elimination *in vivo*. **A,** Diagram of imaging setups used to measure GV contrast in the blood and liver. Inset i, intravascular persistence of purified GVs was visualized by ultrafast power Doppler imaging of the brain. Inset ii, hepatic persistence of GVs modified to produce non-linear contrast was visualized by amplitude modulation imaging of the liver. **B,** Representative power Doppler images of a coronal cross section of the brain following GV injection. Scale bars, 2 mm. **C-D,** Normalized time courses of ultrafast Doppler signal enhancement in the brain (**C**, N = 6) and AM signal in the liver (**D**, N = 4). Dashed lines, time of GV injection (300 s); thin lines, individual trials; thick lines, mean; shaded areas, ± SEM. **E,** Representative AM images of a liver cross section following GV injection. Scale bars, 2 mm. **F,** Biodistribution of fluorescently-labeled GVs 1 h after IV injection. Representative fluorescence image of excised organs (left; scale bar, 10 mm). Percentage of total collected photons originating from each organ (right). N = 5. Error bars not shown.

Gas vesicle blood clearance, liver uptake and degradation can be monitored by ultrasound. We started by quantifying the kinetics of GV uptake and degradation in healthy C57BL/6 mice (**Fig. 1a**). We first visualized intravascular GVs with ultrafast power Doppler imaging, leveraging the ability of intravenously (IV) injected GVs to enhance blood flow contrast.[25] We chose the brain as our target organ due to its practical advantages in mouse experiments: hemodynamic signals can be conveniently measured through intact skin and skull[25,37] and head-fixation reduces motion artifacts. We acquired images of a single coronal plane at a center frequency of 15 MHz and frame rate of 0.25 Hz (**Fig. 1b**). Following a 300-s baseline, we IV injected 100 µL of purified GVs isolated from *Anabaena flos-aquae* (OD_{500}30, corresponding to 2.1 x 10^{11} particles[20]) and tracked the ensuing distribution and clearance (**Fig. 1c**). As expected, the introduction of GVs caused a marked increase in hemodynamic signal, peaking at approximately 100 s after injection, and returning to baseline with an apparent circulation half-life of 232 s (**Fig. 1c, Fig. S1**).

Next, we quantified GV uptake and degradation in the liver by imaging this organ during and after IV injection (**Fig. 1a**). To maximize GV specificity, we injected GVs modified to produce non-linear ultrasound contrast[27] and imaged with a non-linear amplitude modulation (AM) pulse sequence[24] (**Fig. 1, d-e**). Following injection of 100 µL GVs at OD_{500} 30, we observed the accumulation of non-linear contrast in the liver—reaching a maximum after approximately 10 min—followed by a gradual loss of signal until only 10% remained at the end of one hour (**Fig. 1d**). Notably, the maximum occurs just as contrast in the blood returns to baseline (**Fig. S2**). The apparent half-life of GVs in the liver—20 min—is substantially longer than their circulation time, and on a timescale consistent with lysosomal processing.[38-40] To independently confirm liver uptake, we acquired fluorescence images of mouse organs excised 1h after IV injection of GVs labeled with a far-red fluorescent dye (**Fig. 1f**). In line with previous investigations of GV biodistribution,[32,33] the liver was the dominant organ for GV uptake, emitting 81.4% of collected photons. The lungs (7.8%) and spleen (5.5%) had minor roles in GV clearance, while the heart and kidneys had no discernible role.

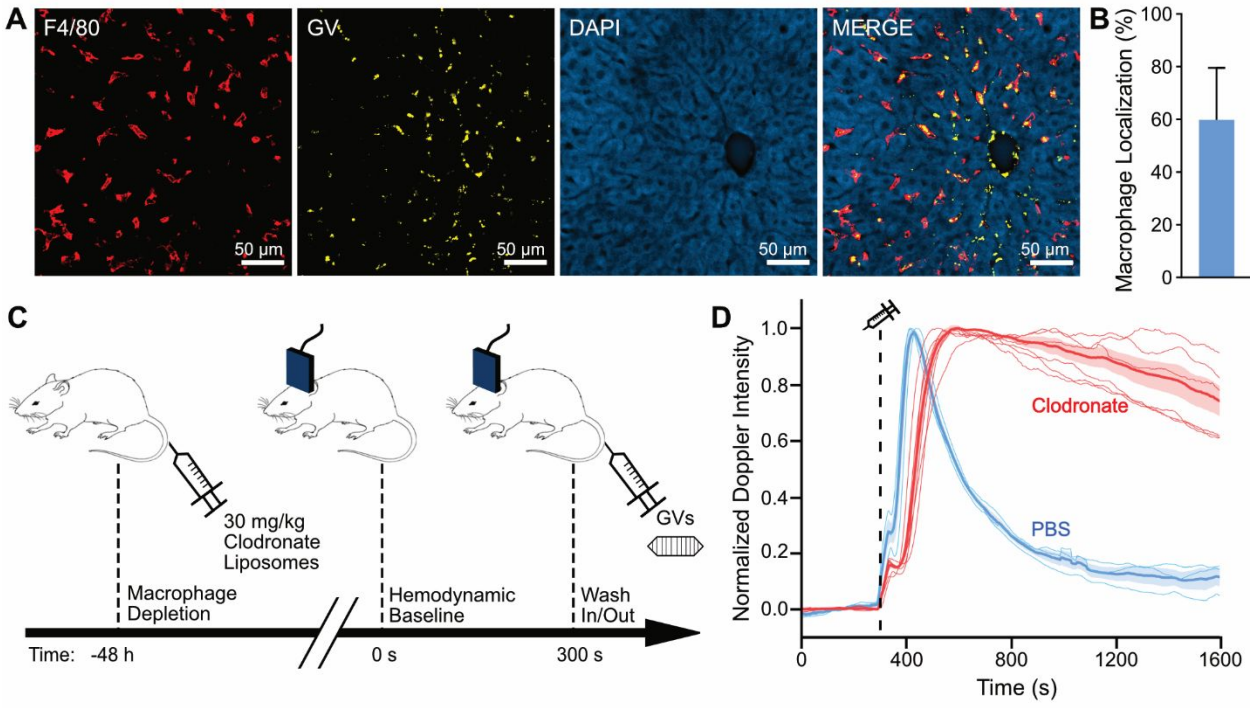

Figure 2: Liver macrophages are the primary mediators of GV clearance. **A,** Immunofluorescent confocal micrographs of 75-μm sections of liver tissue obtained from healthy mice 1h after IV injection of fluorescently-labeled GVs. Sections were stained with anti-F4/80 (macrophages) and DAPI. Scale bars, 50 μm. **B,** Percentage of detected GVs found within macrophage regions based on segmentation with ilastik. Error bars indicate ± SD. N = 3 biological replicates, 78 total fields of view. **C,** Experimental timeline. Macrophages were depleted by IV injection of 30 mg/kg liposomal clodronate 48 h before GV injection. **D,** Normalized Doppler signal enhancement time courses following IV injection of GVs in mice pre-treated with clodronate (red, N = 6) or saline liposomes (blue, N = 3). Dashed line, time of GV injection (300 s); thin lines, individual trials; thick lines, mean; shaded areas, ± SEM.

GVs are primarily cleared by liver macrophages. To identify the cells involved in GV clearance, we performed immunofluorescence imaging of liver sections obtained from mice perfused 1h after IV injection of fluorescently-labeled GVs (**Fig. 2a**). Based on the apparent active degradation of GVs, as suggested by the gradual decline of liver ultrasound contrast, we hypothesized that GVs would be taken up by Kupffer cells—resident macrophages lining the hepatic sinusoids which are implicated in the clearance of many nanoparticles.[7] We tested this hypothesis by defining antibody-stained F4/80$^+$ Kupffer cell regions through image segmentation by Ilastik[41] and quantifying the localization of GVs with respect to these borders (**Fig. S3**). On average, 60% of GV-containing pixels resided within Kupffer cells (**Fig. 2b**).

To confirm the role of Kupffer cells in GV clearance, we ablated phagocytic cells by IV administration of 30 mg/kg liposome-encapsulated clodronate[42] (**Fig. 2c**). 48h later, we measured GV circulation times with hemodynamic ultrasound (**Fig. 2d**). Compared to mice treated with saline-filled control liposomes, clodronate-treated mice had a nearly 7-fold enhancement in GV circulation time, with half-life increasing from 274 s to 1670 s (**Fig. S2**). Our results are in line with previous observations that treatment with 50 mg/kg clodronate increased the circulation half-life

of 100 nm gold nanoparticles 13-fold.[1] Taken together, our data shows that GVs are mainly filtered from the blood by Kupffer cells.

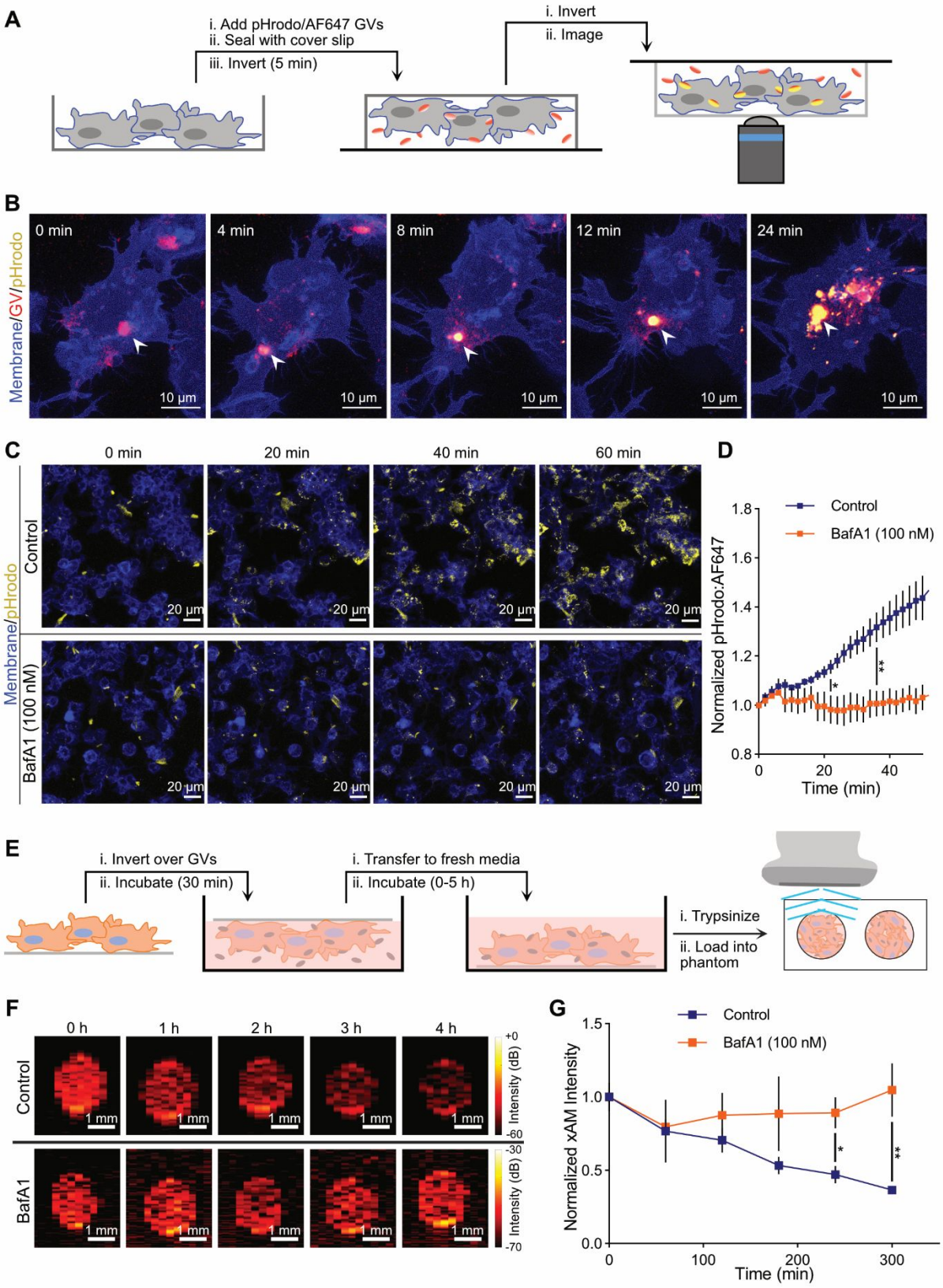
A
i. Add pHrodo/AF647 GVs
ii. Seal with cover slip
iii. Invert (5 min)
i. Invert
ii. Image
B
Membrane/GV/pHrodo
0 min
4 min
8 min
12 min
24 min
10 μm
C
0 min
20 min
40 min
60 min
Membrane/pHrodo
Control
BafA1 (100 nM)
20 μm
D
Control
BafA1 (100 nM)
Normalized pHrodo:AF647
Time (min)
E
i. Invert over GVs
ii. Incubate (30 min)
i. Transfer to fresh media
ii. Incubate (0-5 h)
i. Trypsinize
ii. Load into phantom
F
0 h
1 h
2 h
3 h
4 h
Control
BafA1
1 mm
Intensity (dB)
G
Control
BafA1 (100 nM)
Normalized xAM Intensity
Time (min)

Figure 3: Internalized GVs are degraded within lysosomes, resulting in loss of ultrasound contrast. **A,** Diagram of live cell confocal microscopy protocol. Murine macrophages (RAW264.7) expressing membrane-localized fluorescent protein (blue) were incubated with GVs dually-labeled with AF647 (red) and pHrodo (yellow) to track localization and pH, respectively. **B,** Representative images of a single cell at different time points following GV uptake. A phagosome maturation event is indicated by the white arrows. Scale bars, 10 μm (63x objective). **C,** Representative population-level images of cells pre-treated with DMSO (top) or 100 nM bafilomycin A1 (bottom) following GV uptake. The AF647 channel is not shown. Scale bars, 20 μm (20x objective). **D,** Ratio of pHrodo to AF647 signals in images from **c**, normalized to the initial timepoint. Error bars represent ± SEM. N = 4. Welch's t test (*: $p<0.05$; **: $p<0.001$). **E,** Diagram of uptake protocol for ultrasound imaging. RAW264.7 cells were incubated for 30 min with GVs modified to produce non-linear signal, transferred to GV-free media for predetermined periods of time, and loaded into an agarose phantom for non-linear xAM imaging. **F,** Representative xAM images of cell pellets pre-treated with DMSO (top) or 100 nM bafilomycin A1 (bottom) at the indicated times after GV uptake. Scale bars, 1 mm. **G,** Time course of xAM signal intensity in cell pellets, normalized to the initial timepoint. Error bars represent ± SEM. N = 4-10 per timepoint. Welch's t-test (*: $p<0.05$; **: $p<0.01$).

GVs are degraded in the lysosome following phagocytosis. Having established their uptake by liver macrophages, we next studied what happens to GVs following phagocytosis. Macrophages typically internalize nanoparticles into membrane-bound organelles—phagosomes—that are then trafficked along the phagolysosomal pathway. During this maturation process, the phagosomes acquire v-ATPase proton pumps to acidify their contents prior to fusion with the lysosome;[43] this low pH environment is required for lysosomal enzyme activity. To visualize the movement of GVs along this pathway *in vitro*, we incubated murine macrophages (RAW264.7) with a dilute suspension of GVs dually-labeled with Alexa Fluor (AF647) and pHrodo

Red—a pH-sensitive dye that fluoresces weakly at pH 7 and brightly at pH 3—and imaged them with live-cell confocal optical microscopy (**Fig. 3a**). Focusing on individual cells, we initially observed punctate spots of AF647 signal, likely corresponding to GVs concentrated within phagosomes, which matured over the next several minutes to produce strong pHrodo signal, indicating acidification of their environment (**Fig. 3b**). Zooming out to observe population-level dynamics revealed that the proportion of GVs in acidified compartments, as parametrized by the ratio of pHrodo to AF647 signal, grew continuously during a 1-hour incubation (**Fig. 3, c-d**). This rise was abolished when v-ATPase was inhibited by pretreatment with 100 nM bafilomycin A1 (BafA1),[44] thereby confirming that GVs undergo phagolysosomal processing in macrophages.

Lysosomal proteolysis is expected to break down the GV shell, resulting in GV collapse, gas dissolution and the disappearance of ultrasound contrast. To confirm this effect *in vitro*, we exposed RAW264.7 cells to GVs for 30 min. At predetermined time intervals, we detached the cells from their solid substrate and loaded them into an agarose phantom for imaging with a non-linear cross-propagating amplitude modulation pulse sequence (xAM)[26] (**Fig. 3e**). In control cells pretreated with 0.01% v/v dimethyl sulfoxide (DMSO), the signal declined with a half-life of approximately 3 h (**Fig. 3, f-g**). Conversely, in cells pretreated with BafA1 to block the activity of the pH-dependent lysosomal enzymes, we observed signal that persisted for at least 5 h without decay. These results confirm that GVs are digested within macrophage lysosomes in a process that can be monitored with non-linear ultrasound imaging. The reason that this process happens somewhat more slowly *in vitro* compared to the liver may be the accelerated rate of phagosome maturation in primary macrophages.[45]

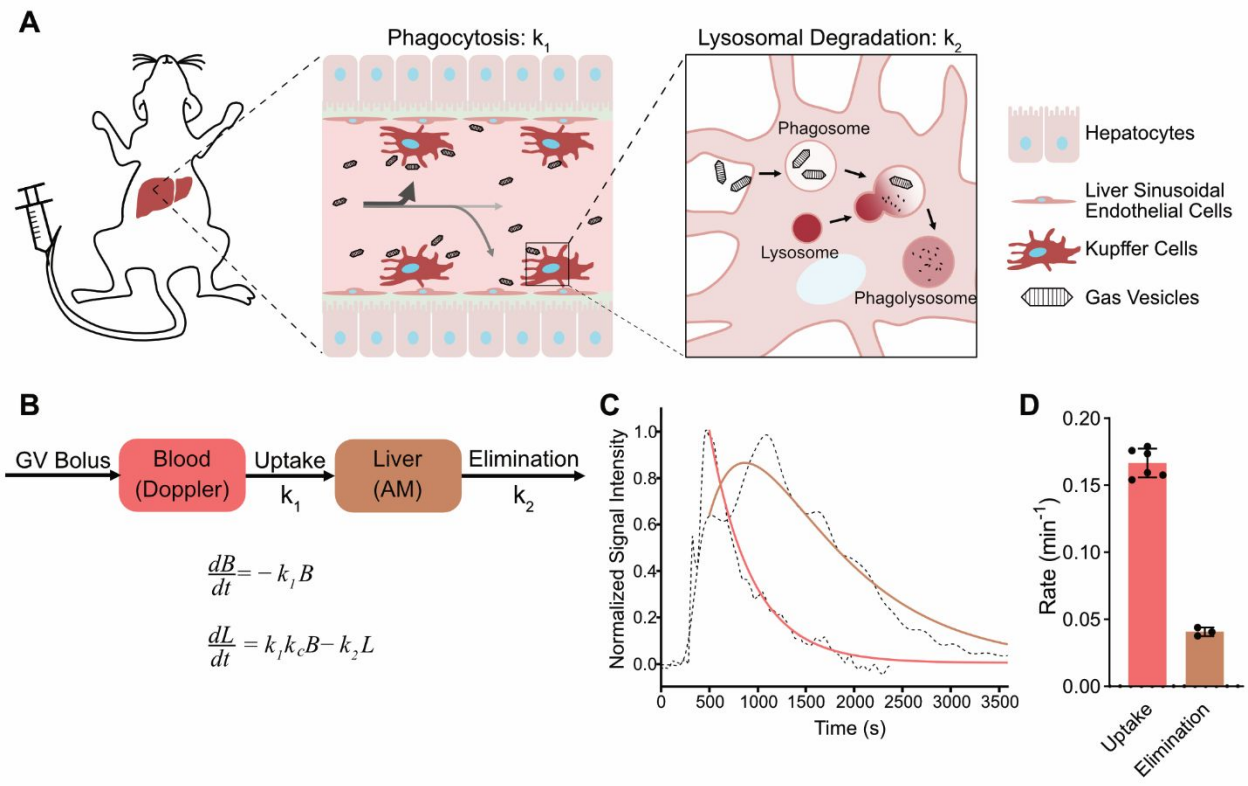

Figure 4: Quantification of phagocytic and lysosomal activities in mouse liver macrophages. **A,** Proposed GV clearance pathway. Upon IV infusion, GVs are phagocytosed from the blood by liver-resident macrophages and degraded by lysosomal proteolysis. **B,** Pharmacokinetic model of GV clearance. Fitting this model to GV signal time courses enables quantification of macrophage function. Uptake and degradation rates are represented by k_1 and k_2, respectively, and k_c is a correction factor that enables conversion between the two imaging modes and accounts for uptake in other tissues. **C,** Representative plot of vascular and liver ultrasound signal time courses in healthy mice (dashed lines) and corresponding fitted curves (solid lines). **D,** Uptake and elimination rates obtained by fitting model to data from Fig. 1, c-d. Error bars represent ± SD.

GV pharmacokinetics can be used to monitor disease progression. The results presented thus far confirm that upon IV injection, GVs are filtered from the blood by liver macrophages and

subsequently catabolized in the lysosome (**Fig. 4a**). This process can be described with a two-compartment pharmacokinetic model comprising the blood and liver, whose rate constants parametrize the concurrent processes of phagocytosis and lysosomal degradation (**Fig. 4b**), with contrast enhancement linearly proportional to intact GV concentration in each compartment (**Fig. S4**). By fitting this model to the dynamics of GV ultrasound contrast in the vasculature and liver *in vivo*, we can thus non-invasively quantify macrophage phagolysosomal function (**Fig. 4c**, input data shown in **Fig. S5**). The assumption that ultrasound signal time courses are representative of true pharmacokinetics is based on two key observations: GVs are stable under our imaging parameters, so changes in signal are due to active biological processes; and GVs are primarily taken up by liver macrophages, with increases in liver AM contrast matched by decreases in brain Doppler contrast. For simplicity, we further assume each process to be first-order and neglect the initial distribution dynamics during GV infusion by considering timepoints occurring after the peak in Doppler signal. Using this approach, we calculated rates of 0.167 min^{-1} and 0.041 min^{-1} for uptake and degradation, respectively, in healthy mice (**Fig. 4d**, **Table S1**).

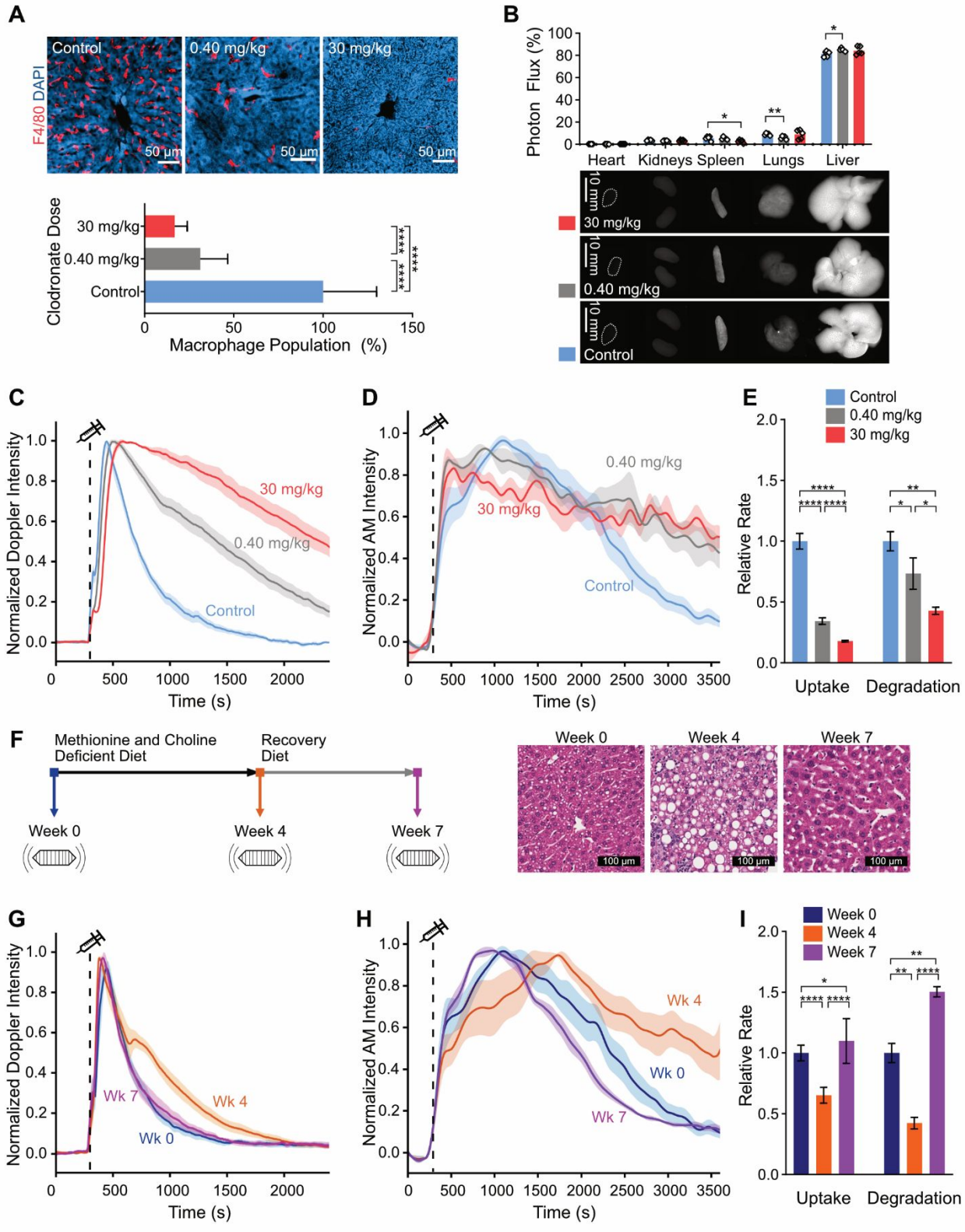
A
Control
0.40 mg/kg
30 mg/kg
F4/80 DAPI
50 μm
Clodronate Dose
30 mg/kg
0.40 mg/kg
Control
Macrophage Population (%)
B
Photon Flux (%)
Heart
Kidneys
Spleen
Lungs
Liver
10 mm
C
Normalized Doppler Intensity
Time (s)
D
Normalized AM Intensity
E
Relative Rate
Uptake
Degradation
F
Methionine and Choline Deficient Diet
Recovery Diet
Week 0
Week 4
Week 7
100 μm
G
Wk 0
Wk 4
Wk 7
H
I

Figure 5: Monitoring disease progression by functional imaging of phagolysosomal activity. **A,** Macrophage population in response to clodronate dose. Top: Representative immunofluorescence confocal micrographs of liver sections labeled with anti-F4/80 (macrophages) and DAPI. Scale bars, 50 μm. Bottom: Macrophage population determined by segmentation with ilastik, normalized to the mean from control livers. Error bars represent ± SD. N = 3 biological replicates, >100 total fields of view. Welch's t-test (****: $p<0.0001$). **B,** Biodistribution of fluorescently-labeled GVs 1h after injection. Bottom: Representative fluorescence images of excised organs. Due to their low fluorescence, the hearts are circled with dashed lines. Scale bars, 10 mm. Top: Percentage of collected photons originating from each organ. Error bars not shown. N = 5. Welch's t-test (*: $p<0.05$; **: $p<0.001$). **C-D,** Normalized time courses of Doppler signal enhancement in the brain (**C**) and AM signal in the liver (**D**) following GV injection in clodronate-treated mice**.** Dashed lines, time of GV injection (300 s); thick lines, mean; shaded areas, ± SEM. N = 4-6. **E**, Uptake and degradation rates obtained by fitting the model in Fig. 4b to each distinct combination of time courses from **C** and **D**, normalized to those of healthy mice. Error bars represent ± SD. Welch's t-test (*: $p<0.05$; **: $p<0.01$; ***: $p<0.001$; ****: $p<0.0001$). **F,** Left: Timeline of NAFLD induction. Mice were fed with a methionine and choline deficient diet for 4 weeks, followed by an additional 3 weeks with a control diet. Right: Representative images of H&E stained liver sections. Scale bars, 100 μm. **G-H,** Normalized time courses of Doppler signal enhancement in the brain (**G**) and AM signal in the liver (**H**) following GV injection in mice with NAFLD. Dashed lines, time of GV injection (300 s); thick lines, mean; shaded areas, ± SEM. N = 4-5. **I,** Uptake and degradation rates obtained by fitting the model in Fig. 4b to the time courses in **G** and **H**, normalized to those of healthy (Week 0) mice. Error bars represent ± SD. Welch's t-test (**: $p<0.01$; n.s: $p>0.05$).

Having established a method to quantify liver macrophage function, we next evaluated its ability to detect pathological disruption of the RES. First, we administered two doses of liposomal

clodronate—0.40 mg/kg and 30 mg/kg—to partially or fully deplete Kupffer cells in the liver. Histological evaluation confirmed that 31% of the Kupffer cell population remained at the lower dose, decreasing to 16% at the higher dose (**Fig. 5a; Fig. S6**). Interestingly, *ex vivo* imaging of organ fluorescence revealed that most GVs are still cleared by the liver (**Fig. 5b**). However, closer inspection of liver sections with immunofluorescence showed GVs tending to localize to the sinusoidal margins, suggesting uptake by liver sinusoidal endothelial cells (LSECs) (**Fig. S7**). This is consistent with a recent study showing that LSECs upregulate phagocytic activity upon depletion of nearby Kupffer cells.[7] Based on these results, we expected that GVs would circulate longer in the blood in clodronate-treated animals due to diminished phagocytic potential, and that their residence time in the liver would increase due to less efficient lysosomal degradation by non-macrophage cells. Indeed, fitting our model to the normalized hemodynamic Doppler (**Fig. 5c**) and liver AM (**Fig. 5d**) signal time courses yielded uptake and degradation rates substantially lower than those of healthy mice (**Fig. 5e**). Specifically, phagocytosis rates were reduced by 66% and 82% at the low and high doses of clodronate, while proteolysis rates were reduced by 27% and 57%, respectively. Notably, phagocytosis rates were proportional to the macrophage population.

For our second model of RES dysfunction, we imaged mice with NAFLD. This disease is characterized by liver infiltration of pro-inflammatory M1-polarized macrophages[5,46] which have lower phagocytic[13,17,34,47] and lysosomal activities[15] than the normally anti-inflammatory Kupffer cells.[48] We induced NAFLD by feeding mice with a methionine- and choline-deficient (MCD) diet[5,49] and performed ultrasound imaging after 4 weeks of this treatment (**Fig. 5f**). Histological evaluation confirmed the appearance of widespread steatosis, a hallmark of NAFLD (**Fig. 5f**). In line with our hypothesis, diseased mice had significantly suppressed phagocytic and lysosomal functions: uptake rate was reduced by 35% while degradation rate was reduced by 58% (**Fig. 5, g-i**). We verified that these differences are not due to saturation of the smaller livers of MCD mice[50] by GVs (**Fig. S8**). When we simulated therapeutic intervention by reverting to a control diet

for 3 additional weeks, the steatosis subsided (**Fig. 5f**) and phagolysosomal activity returned to its original level (**Fig. 5, g-i**). Compared to age-matched litter-mate controls, these "recovered" mice showed a slight decrease in degradation rate but no discrepancies in uptake rate (**Fig. S9**, **Table S1**). Taken together, our results demonstrate the capability of GV-enhanced ultrasound to non-invasively visualize macrophage malfunction as a biomarker of disease.

Conclusions

GVs are advantageously positioned to image *in vivo* phagolysosomal function due to their inherent stability at ambient conditions, susceptibility to natural proteolytic degradation and dependence on shell integrity for ultrasound contrast. When combined with a simple pharmacokinetic model, GV imaging makes it possible to parametrize macrophage activity in terms of phagocytosis and lysosomal degradation rates, clearly delineating healthy and disease states, as demonstrated in two models of RES deficiency.

The diagnostic power of macrophage functional imaging arises from the dependence of phagolysosomal kinetics on cellular phenotype which, in turn, reflects the local tissue and inflammatory microenvironment. Moving forward, this capability could be refined by application of GVs engineered to display surface ligands,[27] as phenotype-specific responses to certain particle-bound domains may augment differences in degradative behavior.[51] Methods to alter GV biodistribution would enable targeting and functional assessment of macrophages in tissues other than the liver. Additionally, the ability to genetically express GVs[23] could enable study of intracellular proteolytic processes, such as autophagy and proteasomal degradation.

To maximize the translational utility of this technology, three aspects could be improved. First, imaging parameters should be optimized for clinical use. In this study, we separately acquired ultrafast Doppler and non-linear AM images to maximize signal specificity. However, simultaneous multiplexed imaging of blood and liver signals would greatly streamline diagnostic

use. This could be accomplished by intercalating amplitude modulation images with Doppler images of the liver, enabling GV quantitation in both compartments with a single, stationary transducer. Second, while GV administration at doses similar to those used in our experiments does not result in acute, adverse health effects in mice,[19] clinical translation would require formal studies of dose-limiting and long-term toxicity. In addition, to support long-term monitoring of individual subjects, it would be useful to better understand the immunogenicity of GVs and the impact of repeated injections, as the development of antibodies may skew clearance kinetics.[52] Finally, in some applications it may be useful to image GVs with other imaging modalities, such as magnetic resonance imaging[28,29] and optical coherence tomography;[53] adaptation of phagolysosomal imaging to these modalities would facilitate applications where the efficacy of ultrasound may be limited.

In summary, the combination of nanoscale, lysosomally-degradable contrast agents and quantitative ultrasound imaging enables non-invasive assessment of macrophage function as a disease-relevant biomarker. This technology will broaden the diagnostic capabilities of biomolecular ultrasound and motivate further methods for non-invasive characterization of cellular function.

Methods

GV preparation and quantification

Native gas vesicles (GVs) were isolated from *Anabaena flos-aquae* as previously described.[20] Concentrations were measured by optical density (OD) at 500 nm using a spectrophotometer (NanoDrop ND-1000, Thermo Scientific). Stripped GVs were prepared by treatment of native GVs with 6M urea solution followed by two rounds of centrifugally-assisted flotation and removal of the subnatant.[20] Fluorescently-labeled gas vesicles were prepared by mixing GVs at OD 10 in 1x phosphate-buffered saline (PBS) with 6 μM Alexa Fluor 647 NHS Ester (Invitrogen, prepared as

10 mM solution in dimethyl sulfoxide). Dually-labeled GVs were prepared by mixing GVs at OD10 with 6 μM pHrodo Red succinimidyl ester (Invitrogen, prepared as 10 mM solution in dimethyl sulfoxide) and 18 μM Alexa Fluor 647 NHS Ester (Invitrogen, prepared as 10 mM solution in dimethyl sulfoxide). After rotating in the dark at 25°C for 1 h, the reactions were quenched with Tris-HCl. Prior to use, all GVs were buffer exchanged into 1x PBS by two rounds of overnight dialysis through a regenerated cellulose membrane (12-14 kD MWCO, Repligen).

Cell culture

RAW264.7 (TIB-71) and HEK293T (CRL-3216) cells were ordered from the American Type Culture Collection (ATCC). Cells were cultured on tissue culture treated 10-cm dishes in Dulbecco's Modified Eagle Medium (DMEM) supplemented with 10% Fetal Bovine Serum and 1% penicillin/streptomycin.

Lentiviral transduction. Plasmid constructs were designed with SnapGene (GSL Biotech) and assembled with Gibson Assembly reagents from New England Biolabs. Briefly, mWasabi[54] was inserted downstream of a 20-AA palmitoylation tag from GAP43 and expressed under the EF-1α promoter (gift from Dan I. Piraner[55]). This plasmid was then transfected along with third-generation lentiviral vector and helper plasmids (kind gifts from the laboratory of David Baltimore) into HEK293T cells using polyethyleneimine (PEI). Following a 12 h incubation, PEI-containing media was replaced with fresh media supplemented with 10 mM sodium butyrate (Sigma Aldrich). Viral particles were concentrated 48 h later *via* ultracentrifugation. RAW264.7 cells were transduced by spinfection. Briefly, concentrated virus was added to non-tissue culture treated 24-well plates coated with RetroNectin (Takara Bio). Following centrifugation (2,000xg, 2h), 4e5 RAW264.7 cells in 1 mL media were added to each well. The plates were spun again at 900xg for 50 min before transferring to the incubator. The brightest 10% of cells were selected with a BD FACSAria III (BD Biosciences) at the City of Hope Analytical Cytometry Core Facility.

Preparation of fibronectin-treated cover slips. Ethanol sterilized square (22 mm x 22 mm) #1.5H glass cover slips (Thorlabs) were individually placed into the wells of a 6-well plate and immersed

in 2 mL PBS containing 10 μg fibronectin from bovine plasma (Sigma Aldrich) for 2h at room temperature. The fibronectin solution was then aspirated and the plates stored at 4°C until use. Sterile glass-bottom 35mm dishes (MatTek) were similarly coated with 2.5 μg fibronectin in 500 μL PBS.

Animal preparation and disease models

All *in vivo* experiments were performed on male C57BL/6J mice (The Jackson Laboratory) under protocols approved by the Institutional Animal Care and Use Committee at the California Institute of Technology.

Macrophage depletion. Liposome-encapsulated clodronate (Clodrosome, Encapsula NanoSciences) was administered through the lateral tail vein 48 h prior to imaging. Mice receiving a dose of 30 mg/kg were injected with undiluted liposome suspension, while mice receiving the lower dose of 0.40 mg/kg were injected with liposomes diluted 1:100 with sterile saline. Control mice were injected with the equivalent volume of undiluted PBS liposomes (Encapsome, Encapsula NanoSciences).

Diet-induced nonalcoholic fatty liver disease. 8-week old mice were free fed with either a methionine and choline deficient diet (5ADJ, TestDiet) or control diet (5CC7, TestDiet) for up to 4 weeks. Afterwards, all mice were fed the control diet for an additional 3 weeks. Because this dietary protocol often results in dramatic weight loss, the mice were monitored weekly for signs of adverse health. GV pharmacokinetics were measured at 2 weeks, 4 weeks and at the conclusion of the study. Immediately after ultrasound imaging, the mice were fixed *via* sequential transcardial perfusion of PBS and 10% neutral buffered formalin (Sigma Aldrich), and the livers were removed for histological assessment by the UCLA Translational Pathology Core Laboratory. Briefly, 4-μm sections were cut from paraffin-embedded organs, stained with hematoxylin & eosin, and imaged at 20x with a Leica Aperio slide scanner.

Ultrasound imaging

Transcranial ultrafast Doppler imaging. Mice (8-10 weeks old) were maintained under 1.5% isoflurane anesthesia on a temperature-controlled imaging platform with a rectal probe (Stoelting Co.). Following head depilation (Nair) and insertion of a catheter with a 30-g needle into the lateral tail vein (fixed in place with GLUture), the mice were head-fixed in a stereotaxic frame inside a light- and sound-proofed box on an optical table. A 16 MHz transducer (Vermon) connected to a programmable ultrasound scanner (Verasonics Vantage) was coupled to the head through a column of ultrasound gel (centrifuged at 2000xg, 10 min to remove bubbles). The transducer was positioned to capture a full coronal section at an arbitrary plane along the rostrocaudal axis. Once the internal temperature of the mouse stabilized at 37°C, power Doppler images were acquired every 4 s for up to 60 min using a previously described functional ultrasound script with slight modifications.[25] Briefly, the pulse sequence consisted of 11 tilted plane waves (varying from -10 to 10 degrees), each containing 8-half-cycle emissions at a voltage of 15V (900 kPa peak positive pressure measured in free water tank). An ensemble of 250 coherently compounded frames, collected at a framerate of 500 Hz, was then processed through a singular value decomposition filter to isolate blood signals from tissue motion and generate a single power Doppler image. 300 s after the start of imaging, 100 µL OD30 native GVs were infused over 10 s by syringe pump. Pixel-wise signal enhancement was calculated as the ratio of intensity at each time point relative to its mean intensity in the first 75 frames. Time courses were then extracted by averaging signal enhancement within a manually defined region of interest encompassing the whole brain, processed with a 10-sample moving mean filter and normalized to the global maximum.

Liver amplitude modulation imaging. Mice (10-14 weeks) were maintained under 2% isoflurane anesthesia on a mouse heating pad controlled by a rectal probe (TCAT-2LV, Physitemp Instruments). After depilation of the abdomen (Nair) and insertion of a 30-g tail vein catheter, the mice were secured in a supine position with surgical tape. Ultrasound imaging was performed with an 18 MHz, 128-element linear array transducer (L22-14v, Verasonics) mounted on a custom-made manual translation stage and positioned such that the liver was at approximately 8

mm in depth. Once the internal temperature of the mouse stabilized at 37°C, B-mode and amplitude modulation images were simultaneously acquired every 4 s for up to 90 min. All images were reconstructed from 128 focused beam ray lines. Each ray line was transmitted at 18 MHz from a 32-element active aperture with a focal depth of 8 mm and peak positive pressure of 600 kPa (measured in free water tank). B-mode images were reconstructed from a single pulse, while amplitude modulation was implemented by first transmitting a single pulse from the full active aperture, followed by two pulses where the even and odd elements in the active aperture are sequentially silenced.[24] Stripped GVs (OD 30, 100 µL) were manually injected as a bolus after 300 s. Image processing and display were performed by internal Verasonics programs. Time courses were calculated as the average signal intensity within a manually defined rectangular region of interest encompassing the liver. To enable comparison, the time courses were smoothed by robust locally weighted-regression using linear least squares, baseline corrected with respect to the first 75 time points and normalized to the global maximum.

In vitro macrophage imaging. Wild-type RAW264.7 cells were seeded onto fibronectin-coated cover slips (2e6 cells/2mL DMEM). After 24 h, the culture media was exchanged with fresh DMEM containing bafilomycin A1 (100 nM) or vehicle (0.01% v/v DMSO). Media of the same composition was used for all subsequent steps. Following a 1 h pretreatment, a GV suspension composed of 320 µL fresh media and 80 µL stripped GVs (OD10 in PBS) was dropped at the center of a UV-sterilized Parafilm-lined 6-well plate and a cover slip was floated on top, cell-side down. This GV suspension was freshly prepared immediately prior to uptake. After incubation at 37°C for 30 min, the cover slips were transferred to pre-warmed fresh media and incubated for the desired amount of time. The media was then aspirated and the cover slips were gently washed once with 2 mL room temperature PBS. Cells were detached with 500 µL 0.25% trypsin-EDTA (Genesee Scientific), neutralized with 1 mL media, and pelleted by centrifugation (300xg, 5 min, 4°C). From this point on, special care was taken to minimize exposure of the cells to temperatures above 4°C. The pellet was washed once with 1.4 mL ice-cold PBS and resuspended in 50 µL cold serum-

free DMEM with 25 mM HEPES before loading into an ultrasound phantom (1% agarose in PBS). Cell densities were manually counted by hemocytometer.

The phantoms were imaged with a 128-element linear array transducer (L10-4v, Verasonics) mounted on a custom manual translation stage using a previously described cross-propagating amplitude modulation pulse sequence[26] that was modified to acquire single frames. Briefly, each frame consisted of 64 ray lines transmitted at 4V (400 kPa peak positive pressure in water) and 6 MHz from a 65-element aperture. Within the active aperture, amplitude modulation was implemented by sequentially sending a plane wave angled at 19.5° from the first 32 elements, a plane wave angled at -19.5° from the last 32 elements, followed by simultaneous emission of both plane waves. The first 3 frames were saved along with a post-collapse image (after 10 insonations at 30 V). Signal intensities were extracted from manually selected circular regions of interest with diameters of 1.8 mm, baseline corrected by subtraction of signal from the post-collapse image, and adjusted for cell density. The time courses from each run were then normalized to the mean intensity from the samples harvested immediately after uptake (t=0).

GV contrast measurement. Phantoms were constructed as previously described.[19] Briefly, phantoms were made by embedding stripped GVs in 1% agarose in PBS and imaged with the same parameters used for liver imaging. Signal intensities were extracted from manually defined regions of interest.

Fluorescence imaging

Whole organ fluorescence. Mice were prepared as described above for transcranial neuroimaging, with the only modification being that the GVs were fluorescently-labeled with Alexa Fluor 647. Ninety minutes after GV injection, the mice were transcardially perfused with 30 mL of cold heparinized PBS (10 U/mL, Sigma Aldrich). The heart, lungs, kidneys, spleen, and liver were then carefully excised and stored in ice-cold Fluorobrite DMEM (Gibco) prior to analysis. Images were acquired on a Bio-Rad ChemiDoc MP imaging system using red epi-illumination and a 695/55 nm

filter with an exposure time of 0.5 s. Integrated intensities were then calculated using the built-in "Analyze Particles" function in FIJI.

Immunofluorescence. Mice were prepared as described above for whole organ fluorescence. Ninety minutes after GV injection, the mice were transcardially perfused with 30 mL of cold heparinized PBS, followed immediately by 20 mL 10% neutral buffered formalin. The liver and spleen were removed and immersed in formalin overnight (4°C). Each organ was then sectioned with a vibrating microtome (75 μm, Compresstome, Precisionary Instruments). Slices were blocked and permeabilized (2h, rt) with PBS containing 10% goat serum (Sigma Aldrich), 0.2% Triton X-100 (Fisher Scientific), and 0.1% sodium azide (Sigma Aldrich). Each slice was stained for macrophages with rat anti-mouse F4/80 (BioLegend, 1:200 dilution, overnight, 4°C) and Alexa Fluor 594 goat anti-rat IgG secondary antibody (2h, rt, 1:400 dilution). The sections were mounted with ProLong Diamond with DAPI (Invitrogen) and allowed to harden overnight before imaging with a Zeiss LSM 800 confocal microscope through a 10x or 20x objective. Imaging parameters prioritized signal specificity over speed.

Confocal microscopy images of entire liver slices were background subtracted in FIJI (20 px, rolling ball method). Randomly selected 500 px by 500 px regions of interest—simulating the sampling of arbitrary fields of view –were exported to Ilastik[41] for processing. The "Density Counting" workflow was used to count macrophages (**Fig. S6**). Images were also segmented into macrophage and non-macrophage regions with the "Pixel Classification" workflow and loaded into MATLAB for colocalization analysis (**Fig. S3**).

Live-cell imaging. 1e5 RAW264.7 cells expressing palmitoylated mWasabi were seeded on fibronectin-treated 35mm glass-bottom dishes. After 24 h, the culture media was exchanged with serum-free Fluorobrite DMEM containing 25 mM HEPES and either 100 nM bafilomycin A1 (Cayman Chemical) or vehicle (0.01% v/v DMSO). Following a 1 h incubation, this media was replaced with a 200 μL freshly-prepared suspension of OD 1.2 dually-labeled GVs. The well was

then sealed with a UV-sterilized 18mm circular glass cover slip and inverted for 5 min at 37°C to allow for contact and uptake.

Laser scanning confocal images were acquired every 2 min for 1h on a Zeiss LSM 800 microscope with a large incubation chamber maintained at 37°C. High magnification images were acquired through a 63x oil immersion objective. Population level images were acquired through a 20x objective. In both cases, acquisition parameters were set to optimize speed. Image files were loaded into FIJI, visualized by maximum intensity projection, de-speckled with a 1-px median filter and quantified by integration of signal intensities across the entire field of view.

Pharmacokinetic modeling

A two-compartment pharmacokinetic model was implemented in MATLAB as the following system of ordinary differential equations:

$$(1)\ \frac{dB}{dt} = -k_1 B$$

$$(2)\ \frac{dL}{dt} = k_1 k_c B - k_2 L$$

Where B represents GV contrast in the blood and L represents GV contrast in the liver. These variables were then directly parametrized with normalized Doppler and AM signal time courses, respectively, and the constants were derived by non-linear least squares curve fitting with initial values of 0 and bounds of 0 to 1. k_1 and k_2 represent rates of phagocytosis and lysosomal degradation, respectively. k_c is a constant relating the blood Doppler signal to the liver nonlinear signal. Input data were all distinct combinations of Doppler and AM time courses from each biological condition. Output values are tabulated in **Table S1**.

Statistical analysis

Sample sizes were chosen based on preliminary experiments to yield sufficient power for the proposed comparisons. Statistical methods are described in applicable figure captions.

Data and code availability

All gas vesicles, plasmids, data and code are available from the authors upon reasonable request.

Author Information

Corresponding Author

*Email: mikhail@caltech.edu

Author Contributions

B.L. and M.G.S. conceived the research. B.L. conducted the *in vivo* imaging experiments with assistance from D. Maresca and A.L.-G. B.L. and J.L. conducted *in vitro* macrophage experiments. B.L. established and validated the pharmacology and disease models with assistance from M.B.S. D. Malounda prepared gas vesicles for experiments. B.L. and M.G.S. wrote the paper with input from all other authors. M.G.S. supervised the research.

Competing interests

The authors declare no competing financial interests.

Acknowledgements

The authors thank A. Collazo and the Caltech Biological Imaging Facility of the Beckman Institute for assistance with optical microscopy; the City of Hope Analytical Cytometry Core Facility for assistance with cell sorting; the UCLA Translational Pathology Core Laboratory for assistance with tissue histology; J. Szablowski for helpful advice on tissue immunofluorescence; L. Frankiw and D. Baltimore for lentiviral plasmids and assistance with macrophage cell lines; and D. Piraner, A. Lakshmanan and D. Wu for fruitful discussions. This research was supported by the National Institutes of Health (grant R01-EB018975 to M.G.S.) and the Human Frontier Science Program (grant RGP0050/2016 to M.G.S.). B.L was supported by the NIH/NRSA Pre-Doctoral Training Grant (T32GM07616) and the Caltech Center for Environmental and Microbial Interactions. J.L. was supported by the Paul and Daisy Soros Fellowship. D.M. was supported by the Human Frontier Science Program Cross-Disciplinary Fellowship (LT000637/2016). Related research in

the Shapiro laboratory is supported by the Pew Charitable Trust, the David and Lucile Packard Foundation and the Heritage Medical Research Institute.

Associated Content

Supporting Information

Figure S1: ultrasound time courses in healthy mice; Figure S2: GV circulation half-life; Figure S3: protocol for image segmentation; Figure S4: linearity of GV contrast; Figure S5: time courses for curve fitting; Figure S6: protocol for cell counting; Figure S7: high-magnification immunofluorescence image of liver sinusoids; Figure S8: validation that GV doses do not cause liver saturation; Figure S9: age-dependence of macrophage activity; Table S1: pharmacokinetic constants.

This material is available free of charge *via* the internet at http://pubs.acs.org.

References

1. Tavares, A. J.; Poon, W.; Zhang, Y.-N.; Dai, Q.; Besla, R.; Ding, D.; Ouyang, B.; Li, A.; Chen, J.; Zheng, G.; Robbins, C.; Chan, W. C. W., Effect of Removing Kupffer Cells on Nanoparticle Tumor Delivery. *Proc. Natl. Acad. Sci. U. S. A.* **2017,** *114*, E10871-E10880.

2. Berg, R. D.; Levitte, S.; O'Sullivan, M. P.; O'Leary, S. M.; Cambier, C.; Cameron, J.; Takaki, K. K.; Moens, C. B.; Tobin, D. M.; Keane, J.; Ramakrishnan, L., Lysosomal Disorders Drive Susceptibility to Tuberculosis by Compromising Macrophage Migration. *Cell* **2016,** *165*, 139-152.

3. Block, M. L.; Zecca, L.; Hong, J.-S., Microglia-Mediated Neurotoxicity: Uncovering the Molecular Mechanisms. *Nat. Rev. Neurosci.* **2007,** *8*, 57-69.

4. Wang, C.; Yue, H.; Hu, Z.; Shen, Y.; Ma, J.; Li, J.; Wang, X.-D.; Wang, L.; Sun, B.; Shi, P.; Wang, L.; Gu, Y., Microglia Mediate Forgetting *via* Complement-Dependent Synaptic Elimination. *Science* **2020,** *367*, 688-694.

5. Kazankov, K.; Jørgensen, S. M. D.; Thomsen, K. L.; Møller, H. J.; Vilstrup, H.; George, J.; Schuppan, D.; Grønbæk, H., The Role of Macrophages in Nonalcoholic Fatty Liver Disease and Nonalcoholic Steatohepatitis. *Nat. Rev. Gastroenterol. Hepatol.* **2019,** *16*, 145-159.

6. Netea, M. G.; Balkwill, F.; Chonchol, M.; Cominelli, F.; Donath, M. Y.; Giamarellos-Bourboulis, E. J.; Golenbock, D.; Gresnight, M. S.; Heneka, M. T.; Hoffman, H. M.; Hotchkiss, R.; Joosten, L. A. B.; Kastner, D. L.; Korte, M.; Latz, E.; Libby, P.; Mandrup-Poulsen, T.; Mantovani, A.; Mills, K. H. G.; Nowak, K. L.*, et al.*, A Guiding Map for Inflammation. *Nat. Immunol.* **2017,** *18*, 826-831.

7. Poon, W.; Zhang, Y.-N.; Ouyang, B.; Kingston, B. R.; Wu, J. L. Y.; Wilhelm, S.; Chan, W. C. W., Elimination Pathways of Nanoparticles. *ACS Nano* **2019,** *13*, 5785-5798.

8. Tsoi, K. M.; MacParland, S. A.; Ma, X.-Z.; Spetzler, V. N.; Echeverri, J.; Ouyang, B.; Fadel, S. M.; Sykes, E. A.; Goldaracena, N.; Kaths, J. M.; Conneely, J. B.; Alman, B. A.; Selzner, M.; Ostrowski, M. A.; Adeyi, O. A.; Zilman, A.; McGilvray, I. D.; Chan, W. C. W., Mechanism of Hard-Nanomaterial Clearance by the Liver. *Nat. Mater.* **2016,** *15*, 1212-1221.

9. Chow, A.; Brown, B. D.; Merad, M., Studying the Mononuclear Phagocyte System in the Molecular Age. *Nat. Rev. Immunol.* **2011,** *11*, 788-798.

10. Blanco, E.; Shen, H.; Ferrari, M., Principles of Nanoparticle Design for Overcoming Biological Barriers to Drug Delivery. *Nat. Biotechnol.* **2015,** *33*, 941-951.

11. Anstee, Q. M.; Reeves, H. L.; Kotsiliti, E.; Govaere, O.; Heikenwalder, M., From NASH to HCC: Current Concepts and Future Challenges. *Nat. Rev. Gastroenterol. Hepatol.* **2019,** *16*, 411-428.

12. Maresca, D.; Lakshmanan, A.; Abedi, M.; Bar-Zion, A.; Farhadi, A.; Lu, G. J.; Szablowski, J. O.; Yoo, S.; Shapiro, M. G., Biomolecular Ultrasound and Sonogenetics. *Annu. Rev. Chem. Biomol. Eng.* **2018,** *9*, 229-252.

13. MacParland, S. A.; Tsoi, K. M.; Ouyang, B.; Ma, X.-Z.; Manuel, J.; Fawaz, A.; Ostrowski, M. A.; Alman, B. A.; Chan, W. C. W.; McGilvray, I. D., Phenotype Determines Nanoparticle Uptake by Human Macrophages from Liver and Blood. *ACS Nano* **2017,** *11*, 2428-2443.

14. Russell, D. G.; VanderVen, B. C.; Glennie, S.; Mwandumba, H.; Heyderman, R. S., The Macrophage Marches on Its Phagosome: Dynamic Assays of Phagosome Function. *Nat. Rev. Immunol.* **2009,** *9*, 594-600.

15. Canton, J.; Khezri, R.; Glogauer, M.; Grinstein, S., Contrasting Phagosome pH Regulation and Maturation in Human M1 and M2 Macrophages. *Mol. Biol. Cell* **2014,** *25*, 3330-3341.

16. Iijima, H.; Moriyasu, F.; Tsuchiya, K.; Suzuki, S.; Yoshida, M.; Shimizu, M.; Sasaki, S.; Nishiguchi, S.; Maeyama, S., Decrease in Accumulation of Ultrasound Contrast Microbubbles in Non-Alcoholic Steatohepatitis. *Hepatol. Res.* **2007,** *37*, 722-730.

17. Yoshikawa, S.; Iijima, H.; Saito, M.; Tanaka, H.; Imanishi, H.; Yoshimoto, N.; Yoshimoto, T.; Futatsugi-Yumikura, S.; Nakanishi, K.; Tsujimura, T.; Nishigama, T.; Kudo, A.; Arii, S.; Nishiguchi, S., Crucial Role of Impaired Kupffer Cell Phagocytosis on the Decreased Sonazoid-Enhanced Echogenicity in a Liver of a Nonalcoholic Steatohepatitis Rat Model. *Hepatol. Res.* **2010,** *40*, 823-831.

18. Walsby, A. E., Gas Vesicles. *Microbiol. Rev.* **1994,** *58*, 94-144.

19. Shapiro, M. G.; Goodwill, P. W.; Neogy, A.; Yin, M.; Foster, F. S.; Schaffer, D. V.; Conolly, S. M., Biogenic Gas Nanostructures as Ultrasonic Molecular Reporters. *Nat. Nanotechnol.* **2014,** *9*, 311-316.

20. Lakshmanan, A.; Lu, G. J.; Farhadi, A.; Nety, S. P.; Kunth, M.; Lee-Gosselin, A.; Maresca, D.; Bourdeau, R. W.; Yin, M.; Yan, J.; Witte, C.; Malounda, D.; Foster, F. S.; Schröder,

L.; Shapiro, M. G., Preparation of Biogenic Gas Vesicle Nanostructures for Use as Contrast Agents for Ultrasound and MRI. *Nat. Protoc.* **2017,** *12*, 2050-2080.

21. Bourdeau, R. W.; Lee-Gosselin, A.; Lakshmanan, A.; Farhadi, A.; Ravindra Kumar, S.; Nety, S. P.; Shapiro, M. G., Acoustic Reporter Genes for Noninvasive Imaging of Microorganisms in Mammalian Hosts. *Nature* **2018,** *553*, 86-90.

22. Farhadi, A.; Ho, G. H.; Kunth, M.; Ling, B.; Lakshmanan, A.; Lu, G. J.; Bourdeau, R. W.; Schröder, L.; Shapiro, M. G., Recombinantly Expressed Gas Vesicles as Nanoscale Contrast Agents for Ultrasound and Hyperpolarized MRI. *AICHE J.* **2018,** *64*, 2927-2933.

23. Farhadi, A.; Ho, G. H.; Sawyer, D. P.; Bourdeau, R. W.; Shapiro, M. G., Ultrasound Imaging of Gene Expression in Mammalian Cells. *Science* **2019,** *365*, 1469-1475.

24. Maresca, D.; Lakshmanan, A.; Lee-Gosselin, A.; Melis, J. M.; Ni, Y.-L.; Bourdeau, R. W.; Kochmann, D. M.; Shapiro, M. G., Nonlinear Ultrasound Imaging of Nanoscale Acoustic Biomolecules. *Appl. Phys. Lett.* **2017,** *110*, 073704.

25. Maresca, D.; Payen, T.; Lee-Gosselin, A.; Ling, B.; Malounda, D.; Demene, C.; Tanter, M.; Shapiro, M. G., Acoustic Biomolecules Enhance Hemodynamic Functional Ultrasound Imaging of Neural Activity. *NeuroImage* **2020,** *209*, 116467.

26. Maresca, D.; Sawyer, D. P.; Renaud, G.; Lee-Gosselin, A.; Shapiro, M. G., Nonlinear X-Wave Ultrasound Imaging of Acoustic Biomolecules. *Phys. Rev. X* **2018,** *8*, 041002.

27. Lakshmanan, A.; Farhadi, A.; Nety, S. P.; Lee-Gosselin, A.; Bourdeau, R. W.; Maresca, D.; Shapiro, M. G., Molecular Engineering of Acoustic Protein Nanostructures. *ACS Nano* **2016,** *10*, 7314-7322.

28. Santiesteban, D. Y.; Hallam, K. A.; Yarmoska, S. K.; Emelianov, S. Y., Color-Coded Perfluorocarbon Nanodroplets for Multiplexed Ultrasound and Photoacoustic Imaging. *Nano Res.* **2019,** *12*, 741-747.

29. Sheeran, P. S.; Dayton, P. A., Phase-Change Contrast Agents for Imaging and Therapy. *Curr. Pharm. Des.* **2012,** *18*, 2152-2165.

30. Ferrara, K.; Pollard, R.; Borden, M., Ultrasound Microbubble Contrast Agents: Fundamentals and Application to Gene and Drug Delivery. *Annu. Rev. Biomed. Eng.* **2007,** *9*, 415-447.

31. Cox, D. J.; Thomas, J. L., Ultrasound-Induced Dissolution of Lipid-Coated and Uncoated Gas Bubbles. *Langmuir* **2010,** *26*, 14774-14781.

32. Le Floc'h, J.; Zlitni, A.; Bilton, H. A.; Yin, M.; Farhadi, A.; Janzen, N. R.; Shapiro, M. G.; Valliant, J. F.; Foster, F. S., *In Vivo* Biodistribution of Radiolabeled Acoustic Protein Nanostructures. *Mol. Imaging Biol.* **2018,** *20*, 230-239.

33. Yan, J.; Yin, M.; Foster, F. S.; Démoré, C. E. M., Tumor Contrast Imaging with Gas Vesicles by Circumventing the Reticuloendothelial System. *Ultrasound Med. Biol.* **2020,** *46*, 359-368.

34. Cheong, H.; Lee, S. S.; Lee, J. S.; Kim, J.; Kim, S. W.; Lee, W. J., Phagocytic Function of Kupffer Cells in Mouse Nonalcoholic Fatty Liver Disease Models: Evaluation with Superparamagnetic Iron Oxide. *J. Magn. Reson. Imaging* **2014,** *41*, 1218-1227.

35. Smits, L.; Coolen, B.; Panno, M.; Runge, J.; Nijhof, W.; Verheij, J.; Nieudorp, M.; Stoker, J.; Beuers, U.; Nederveen, A.; Stroes, E., Noninvasive Differentiation between Hepatic Steatosis and Steatohepatitis with MR Imaging Enhanced with USPIOs in Patients with Nonalcoholic Fatty Liver Disease: A Proof-Of-Concept Study. *Radiology* **2016,** *278*, 782-791.

36. Miyata, Y.; Miyahara, T.; Moriyasu, F., Decreased Accumulation of Ultrasound Contrast in the Liver of Nonalcoholic Steatohepatitis Rat Model. *World J. Gastroenterol.* **2011,** *17*, 4191-4198.

37. Macé, E.; Montaldo, G.; Cohen, I.; Baulac, M.; Fink, M.; Tanter, M., Functional Ultrasound Imaging of the Brain. *Nat. Methods* **2011,** *8*, 662-664.

38. Oh, Y.-K.; Swanson, J. A., Different Fates of Phagocytosed Particles after Delivery Into Macrophage Lysosomes. *J. Cell Biol.* **1996,** *132*, 585-593.

39. Davidson, S. J., Proteolytic Activity within Lysosomes and Turnover of Pinocytic Vesicles. A Kinetic Analysis. *Biochim. Biophys. Acta, Gen. Subj.* **1975,** *411*, 282-290.

40. Harashima, H.; Hirai, N.; Kiwada, H., Kinetic Modelling of Liposome Degradation in Peritoneal Macrophages. *Biopharm. Drug Dispos.* **1995,** *16*, 113-123.

41. Berg, S.; Kutra, D.; Kroeger, T.; Straehle, C. N.; Kausler, B. X.; Haubold, C.; Schiegg, M.; Ales, J.; Beier, T.; Rudy, M.; Eren, K.; Cervantes, J. I.; Xu, B.; Beuttenmueller, F.; Wolny, A.; Zhang, C.; Koethe, U.; Hamprecht, F. A.; Kreshuk, A., Ilastik: Interactive Machine Learning for (Bio)image Analysis. *Nat. Methods* **2019,** *16*, 1226-1232.

42. van Rooijen, N.; Hendrikx, E., Liposomes for Specific Depletion of Macrophages from Organs and Tissues. *Methods Mol. Biol.* **2010,** *605*, 189-203.

43. Kinchen, J. M.; Ravichandran, K. S., Phagosome Maturation: Going through the Acid Test. *Nat. Rev. Mol. Cell Biol.* **2008,** *9*, 781-795.

44. Yoshimori, T.; Yamamoto, A.; Moriyama, Y.; Futai, M.; Tashiro, Y., Bafilomycin A1, a Specific Inhibitor of Vacuolar-Type H^+-ATPase, Inhibits Acidification and Protein Degradation in Lysosomes of Cultured Cells. *J. Biol. Chem.* **1991,** *266*, 17707-17712.

45. Guo, M.; Hartlova, A.; Dill, B. D.; Prescott, A. R.; Gierlinski, M.; Trost, M., High-Resolution Quantitative Proteome Analysis Reveals Substantial Differences between Phagosomes of RAW264.7 and Bone Marrow Derived Macrophages. *Proteomics* **2015,** *15*, 3169-3174.

46. Kassel, K. M.; Guo, G. L.; Tawfik, O.; Luyendyk, J. P., Monocyte Chemoattractant Protein-1 Deficiency Does Not Affect Steatosis or Inflammation in Livers of Mice Fed a Methionine-Choline-Deficient Diet. *Lab. Invest.* **2010,** *90*, 1794-1804.

47. Asanuma, T.; Ono, M.; Kubota, K.; Hirose, A.; Hayashi, Y.; Saibara, T.; Inanami, O.; Ogawa, Y.; Enzan, H.; Onishi, S.; Kuwabara, M.; Oben, J. A., Super Paramagnetic Iron Oxide MRI Shows Defective Kupffer Cell Function in Non-Alcoholic Fatty Liver Disease. *Gut* **2010,** *59*, 258-266.

48. Heymann, F.; Peusquens, J.; Ludwig-Portugall, I.; Kohlhepp, M.; Ergen, C.; Niemietz, P.; Martin, C.; Van Rooijen, N.; Ochando, J. C.; Randolph, G. K.; Luedde, T.; Ginhoux, F.; Kurts, C.; Trautwein, C.; Tacke, F., Liver Inflammation Abrogates Immunological Tolerance Induced by Kupffer Cells. *Hepatology* **2015,** *62*, 279-291.

49. Hebbard, L.; George, J., Animal Models of Nonalcoholic Fatty Liver Disease. *Nat. Rev. Gastroenterol. Hepatol.* **2011,** *8*, 35-44.

50. Itagaki, H.; Shimizu, K.; Morikawa, S.; Ogawa, K.; Ezaki, T., Morphological and Functional Characterization of Non-Alcoholic Fatty Liver Disease Induced by a Methionine-Choline-Deficient Diet in C57BL/6 mice. *Int. J. Clin. Exp. Pathol.* **2013,** *6*, 2683-2696.

51. Dill, B. D.; Gierlinski, M.; Hartlova, A.; Gonzalez, A. A.; Guo, M.; Clarke, R. G.; Trost, M., Quantitative Proteome Analysis of Temporally Resolved Phagosomes following Uptake *via* Key Phagocytic Receptors. *Mol. Cell. Proteomics* **2015,** *14*, 1334-1349.

52. Abu Lila, A. S.; Kiwada, H.; Ishida, T., The Accelerated Blood Clearance (ABC) Phenomenon: Clinical Challenge and Approaches to Manage. *J. Controlled Release* **2013,** *172*, 38-47.

53. Lu, G. J.; Chou, L.-d.; Malounda, D.; Patel, A. K.; Welsbie, D. S.; Chao, D. L.; Ramalingam, T.; Shapiro, M. G., Genetically Encodable Contrast Agents for Optical Coherence Tomography. *ACS Nano* **2020**.

54. Ai, H.-w.; Olenych, S. G.; Wong, P.; Davidson, M. W.; Campbell, R. E., Hue-Shifted Monomeric Variants of *Clavularia* Cyan Fluorescent Protein: Identification of the Molecular Determinants of Color and Applications in Fluorescence Imaging. *BMC Biol.* **2008,** *6*, 13.

55. Piraner, D. I.; Wu, Y.; Shapiro, M. G., Modular Thermal Control of Protein Dimerization. *ACS Synth. Biol.* **2019,** *8*, 2256-2262.

ToC Graphic

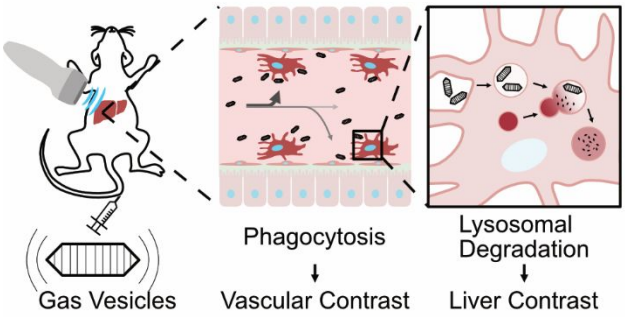
Gas Vesicles
Phagocytosis
Vascular Contrast
Lysosomal Degradation
Liver Contrast